Ground-state electron transfer in all-polymer donor-acceptor heterojunctions

Ground-state electron transfer in all-polymer donor-acceptor heterojunctions

Kai Xu[1], Hengda Sun[1], Tero-Petri Ruoko[1], Gang Wang[1], Renee Kroon[2], Nagesh B. Kolhe[3], Yuttapoom Puttisong[4], Xianjie Liu[1], Daniele Fazzi[5], Koki Shibata[6], Chi-Yuan Yang[1], Ning Sun[7], Gustav Persson[8], Andrew B. Yankovich[8], Eva Olsson[8,9], Hiroyuki Yoshida[10,11], Weimin M. Chen[4], Mats Fahlman[1,12], Martijn Kemerink[13], Samson A. Jenekhe[3], Christian Müller[2,9], Magnus Berggren[1,12]*, Simone Fabiano[1,12]**

[1]Laboratory of Organic Electronics, Department of Science and Technology, Linköping University, 60174 Norrköping, Sweden

[2]Department of Chemistry and Chemical Engineering, Chalmers University of Technology, 41296 Göteborg, Sweden

[3]Department of Chemical Engineering and Department of Chemistry, University of Washington, Seattle, WA 98195, United States

[4]Department of Physics Chemistry and Biology, Linköping University, 58183 Linköping, Sweden

[5]Institut für Physikalische Chemie, Department Chemie, Universität zu Köln, Luxemburger Str. 116, D-50939 Köln, Germany

[6]Graduate School of Science and Engineering, Chiba University, 1-33 Yayoi-cho, Inage-ku, Chiba 263-8522, Japan

[7]Department of Physics, Center for Optoelectronics Engineering Research, Yunnan University, Kunming 650091, China

[8]Department of Physics, Chalmers University of Technology, 41296 Göteborg, Sweden

[9]Wallenberg Wood Science Center, Chalmers University of Technology, 41296 Göteborg, Sweden

[10]Graduate School of Engineering, Chiba University, 1-33 Yayoi-cho, Inage-ku, Chiba 263-8522, Japan

[11]Molecular Chirality Research Center, Chiba University, 1-33 Yayoi-cho, Inage-ku, Chiba 263-8522, Japan

[12]Wallenberg Wood Science Center, Linköping University, 60174 Norrköping, Sweden

[13]Complex Materials and Devices, Department of Physics Chemistry and Biology, Linköping University, 58183 Linköping, Sweden

*hengda.sun@liu.se; magnus.berggren@liu.se; simone.fabiano@liu.se

Doping of organic semiconductors is crucial for the operation and performance of organic (opto)electronic and electrochemical devices. Typically, this is achieved by adding heterogeneous dopant molecules or polyelectrolytes to the polymer bulk. Unfortunately, this often results in poor stability and performance due to diffusion and sublimation of the dopants or aggregation, rendering the bulk partially non-conducting. In small-molecule donor-acceptor semiconductor systems, charge transfer can yield stable electrical conductivities reaching that of metals, an approach that so far has not been explored in all-conjugated polymer systems. Here, we report ground-state electron transfer in a series of all-polymer donor-acceptor heterojunctions. Combining low ionization energy conjugated polymers with high electron affinity counterparts yields conducting interfaces with resistivity values that are 5–6 orders of magnitude lower than those of the separate single-layer polymers. The large decrease in resistivity originates from two parallel quasi-2D electron and hole distributions reaching a concentration of ~10^{13} cm^{-2}. Further, we demonstrate that the concept can be transferred to 3D bulk heterojunctions, displaying exceptional thermal stability due to the absence of molecular dopants. Our findings hold promise for novel electro-active composites of potential use in *e.g.* thermoelectrics and wearable electronics.

Doping is an essential process needed to define and optimize the performance of organic electronic and electrochemical devices. Especially, this is true when high or precise control over the electrical conductivity is required in devices based on in principle intrinsic semiconducting conjugated organic materials[1-5]. Both p- and n-doping are widely utilized in various devices, such as in the charge injection/extraction layers of organic light emitting diodes (OLEDs), organic solar cells (OSCs), and organic field effect transistors (OFETs), as well as in the active materials of thermoelectric generators and electrochemical transistors[3-10].

Typically, this is done by the addition of heterogeneous dopant molecules or polyelectrolytes that, once the electrical doping process is completed, not only become redundant but often negatively affect both the electrical and mechanical properties of the semiconductor through generation of non-conducting phases inside the doped bulk[11,12], or reduction of the mobility due to Coulomb scattering[13,14]. While many polymer:dopant systems exist that are stable upon mild thermal annealing, more rapid diffusion and sublimation occurs at higher temperatures[15], which can ultimately lead to degradation of the electrical properties[16-20].

Intuitively, if one brings two different semiconducting polymers in physical contact and if the electron affinity (EA) of one (acceptor, A) polymer matches the ionization energy (IE) of the other (donor, D) polymer at the interface[21], electron transfer from D to A may occur spontaneously in the electronic ground state, without any external excitation or charge injection. By its nature, such a spontaneous process will create an equal number of mobile positive and negative charge carriers, and the process cannot be compared to conventional n- or p-doping where only one type of charge carrier can be mobile. The exclusion of immobile counter charges may be anticipated to solve issues related to stability, phase segregation, and morphology perturbation, features that will negatively impact charge carrier mobility. In small molecule D-A systems, this concept has been demonstrated in the form of charge transfer (CT) salts, resulting in conducting systems with metallic transport properties[22]. However, CT salts either suffer from poor film forming capabilities[23,24], or they rely on the use of single crystals[25,26], and have therefore limited practical applications. The use of all-polymer electron transfer heterojunctions could potentially solve these issues. However, while previously debated[27], ground state electron transfer (GSET) in all-polymer blends has not been realized.

Herein, we report a systematic study of GSET in all-polymer D-A heterojunctions, providing a novel approach for generating highly mobile charges in polymer semiconductors. We find that conducting interfaces with resistivities of around 2 MΩ/sq. are obtained when

high-EA electron-transporting (acceptor) polymers, such as poly(benzimidazobenzophenanthroline) (BBL), are combined with low-IE hole-transporting (donor) polymers, such as bithiophene-thiophene (P($g_4$2T-T)) or bithiophene-thienothiophene (P($g_4$2T-TT)) co-polymers, carrying oligoethylene glycol side chains (Fig. 1a). Two parallel quasi-2D electron and hole distributions, each reaching a concentration of 10^{13} cm^{-2}, are confined to nanometer-thin layers and hence correspond to an electrical conductivity of about 2 S/cm. The remarkable vacuum level shift and spin signals observed in UPS and EPR measurements, respectively, are attributed to the formation of polarons induced by spontaneous electron transfer at the D-A heterointerfaces. UV-Vis absorption spectra, combined with quantum-chemical calculations, further revealed that both negative and positive polarons are present in the bilayer. It can be anticipated that our discovery of all-polymer GSET will have a similar impact on the field of organic electronics as the discovery of all-polymer excited state CT in the context of OLEDs and OSCs[28,29].

The energetics of the bilayers were studied by ultraviolet photoelectron spectroscopy (UPS) and low-energy inverse photoelectron spectroscopy (LEIPS)[30,31]. The resulting energy level diagrams are given in Fig. 1b. BBL films were prepared on a series of conducting substrates (Al, Au, ITO, PEDOT:PSS) spanning a range of work functions (WFs). The resulting BBL/substrate WF (4.50±0.04 eV) and BBL IE (6.33±0.04 eV) were found to be substrate-independent (Supplementary Fig. 1). The substrate-independent WF suggests the existence of a free charge density in the as-prepared BBL films that is sufficiently large to equilibrate the Fermi level (chemical potential) across the BBL/substrate interface. From the LEIPS measurements, the EA of BBL was determined to be 4.15±0.02 eV (Supplementary Fig. 2). Films of the two donors P($g_4$2T-T) and P($g_4$2T-TT), as well as of the corresponding polymers carrying alkyl side chains, namely poly(3-hexylthiophene) (P3HT) and poly[2,5-bis(3-tetradecylthiophen-2-yl)thieno[3,2-b]thiophene] (PBTTT), were spin-cast on a series of

high WF substrates to obtain their so-called positive pinning energies (E_{ICT+}). The latter, also derivable through computational approaches[32-34], can then be used to predict the energy level alignment, including the size and direction of the vacuum level shift, at weakly-interacting organic semiconductor interfaces[35,36]. A second series of films were then fabricated on identically prepared BBL/PEDOT:PSS/ITO substrates and the resulting change in WF was measured using UPS for each donor polymer (Supplementary Fig. 3), thereby obtaining an estimate of the vacuum level shift (Fig. 1b). The obtained WFs and vacuum level shifts are in excellent agreement with estimates based on the measured donor polymer E_{ICT+} values. P3HT/BBL and PBTTT/BBL interfaces show almost identical vacuum level shifts (0.45 eV), indicating a similar amount of electron transfer from the two donors to BBL. For P($g_4$2T-TT)/BBL and P($g_4$2T-T)/BBL, the vacuum level shifts are larger than for P3HT/BBL and PBTTT/BBL, with values of 0.50 eV and 0.55 eV, respectively. Hence, the UPS data show that GSET is stronger for P($g_4$2T-T) followed by P($g_4$2T-TT), while P3HT and PBTTT yield the least GSET.

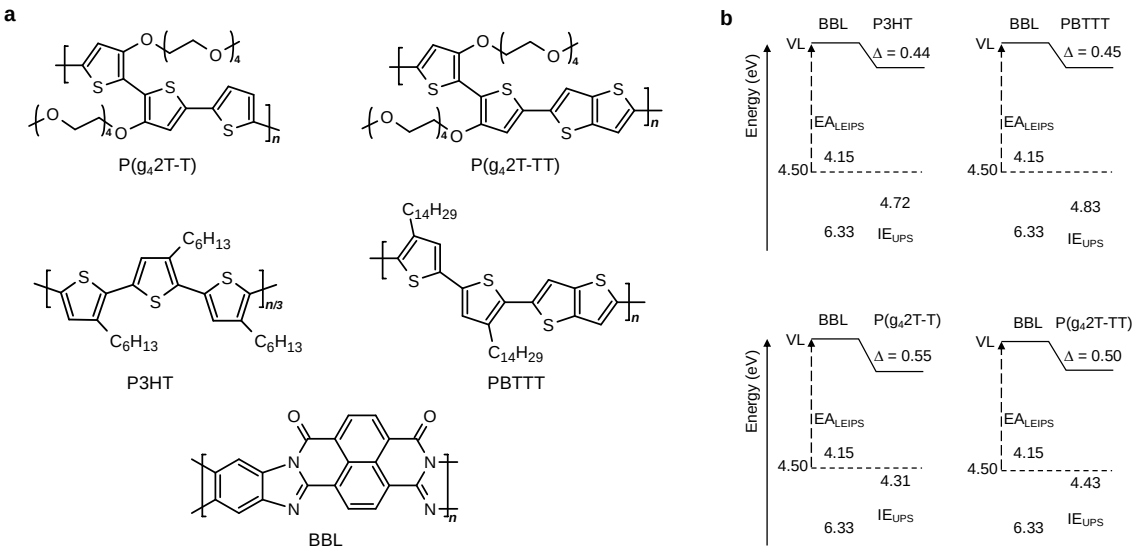

Fig. 1 | Energetics of the all-polymer D-A heterojunctions. a, Chemical structures of P($g_4$2T-T), P($g_4$2T-TT), P3HT, PBTTT and BBL. **b**, Energy level diagrams of the all-polymer D-

A heterojunctions as obtained by UPS and LEIPS (EA = electron affinity; IE = ionization energy). The resulting down-shift (Δ, in eV) of the vacuum level (VL) for P3HT/BBL, PBTTT/BBL, P($g_4$2T-T)/BBL, and P($g_4$2T-TT)/BBL heterojunctions is reported in the diagram.

Bilayer films were prepared by spin coating the donor polymers on top of BBL films from orthogonal solvents (see Methods for further details). This results in a 2D interface between the donor and acceptor polymers (Supplementary Figs. 4 and 5). Grazing-incidence wide-angle X-ray scattering shows that the bilayer diffraction pattern is predominantly a superposition of both donors and acceptor patterns (Supplementary Figs. 6 and 7). Fig. 2a shows representative current–voltage (I–V) characteristics of pristine BBL, P($g_4$2T-T), and P($g_4$2T-TT) films as well as P($g_4$2T-T)/BBL and P($g_4$2T-TT)/BBL bilayer films measured at room temperature in a two-terminal lateral device configuration (Fig. 2a, inset). We measured 10 devices for each kind of pristine polymer and bilayer film, all exhibiting an excellent level of device-to-device reproducibility. In all cases, the I–V curves show a linear response without any noticeable limitations from the electrical contacts. Moreover, the comparison of two- and four-terminal measurements, which show comparable resistivity values, indicates that the contact resistance can be neglected (Supplementary Fig. 8). The average sheet resistances are shown in Fig. 2b. The room-temperature resistance measured on individual ~20 nm thin films of each polymer is typically larger than 100 GΩ/sq. In contrast, when P($g_4$2T-T) and P($g_4$2T-TT) are spin-coated on top of BBL to form bilayers, the resistance drops by more than five orders of magnitude as compared to the pristine films, now reaching a value of 2.3±0.4 MΩ/sq. Note that the latter value reflects the charge transport in a single quasi-2D interfacial layer, resulting in an electrical conductivity of about 2 S/cm as detailed below. This large drop in room-temperature resistance is indicative of a strongly enhanced

conductivity due to interfacial GSET. The resistance is found to be independent of the individual donor and acceptor polymer film thickness (Supplementary Fig. 9), suggesting that GSET is limited to the first few molecular layers on either side of the interface (cf. kinetic Monte Carlo simulations below)[22]. For comparison, we measured the changes in resistance when donor polymers with high IE (P3HT and PBTTT) were spin-coated on top of the BBL layer. The room-temperature resistance of the resulting bilayers varied by less than 3 orders of magnitude, reaching values in the range of 300-3000 MΩ/sq. (Supplementary Fig. 10). To assess the impact of the dielectric environment on GSET, we used poly(3-carboxy-pentyl-thiophene) (P3CPT), a conjugated polyelectrolyte having a similar dielectric constant (ε_e = 3.9±0.1) to P($g_4$2T-TT) (4.2±0.1)[37] and P($g_4$2T-T) (4.4±0.2) but higher IE (4.84±0.04 eV) (Supplementary Figs. 3 and 11). When P3CPT was spun on top of BBL, we observed no significant vacuum level shift as well as high resistance values (1.2±0.7 GΩ/sq.) (Supplementary Fig. 10), as in the case of P3HT/BBL and PBTTT/BBL bilayers. In addition, pure tetraethylene glycol, drop-casted on top of BBL, also results in high resistance values (2.1±0.2 GΩ/sq., Supplementary Fig. 12), indicating that a polar environment alone cannot explain the decrease in resistance. The temperature dependence of the resistance for P($g_4$2T-T)/BBL, P($g_4$2T-TT)/BBL, P3HT/BBL, and PBTTT/BBL bilayers is summarized in the Arrhenius plot of Fig. 2c. For a given voltage, the current in P($g_4$2T-T)/BBL and P($g_4$2T-TT)/BBL bilayers decreases as the temperature is lowered from 300 K to 200 K. The linearity of the data for P($g_4$2T-T)/BBL and P($g_4$2T-TT)/BBL interfaces indicates that conduction at the D-A interface is thermally activated. Activation energies of 120±15 meV and 150±13 meV are obtained for electron and hole transport along the P($g_4$2T-T)/BBL and P($g_4$2T-TT)/BBL interfaces, respectively, smaller than those extracted for P3HT/BBL (260±17 meV) and PBTTT/BBL (235±23 meV). This further supports an increase in the carrier density due to GSET when donor polymers with a low IE are used[38].

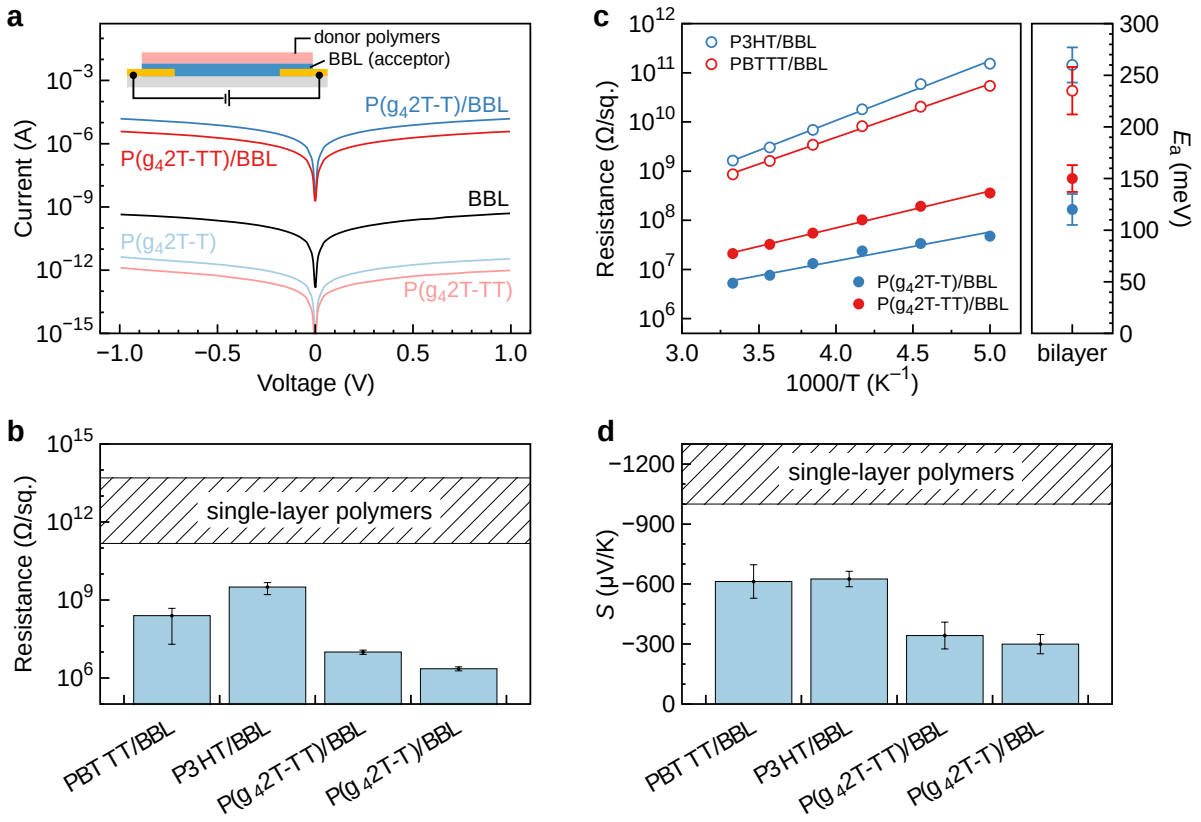

Fig. 2 | Electrical characterization of the all-polymer D-A heterojunctions. a, I–V curves of all-polymer-based devices. The inset shows the two-terminal lateral device configuration used for the measurement. **b**, Column diagram of resistance statistics of BBL, P(g$_4$2T-T), P(g$_4$2T-TT), and the corresponding bilayer films; error bars represent standard deviation. **c**, Resistance of the bilayer film as a function of temperature; error bars represent standard deviation. **d**, Seebeck coefficient of P(g$_4$2T-T)/BBL, P(g$_4$2T-TT)/BBL, P3HT/BBL, and PBTTT/BBL bilayer films; error bars represent standard deviation.

The Seebeck coefficients (*S*) of the polymer combinations also show a similar trend as the 2D conduction and sheet resistance values (Fig. 2d). Because of the high resistivity of the individual polymers, the thermovoltages of the pristine (non-conducting) materials cannot be measured reliably, but they are larger than 1000 μV/K. When P(g$_4$2T-T)/BBL and P(g$_4$2T-TT)/BBL bilayers are formed, their Seebeck coefficients drop to -300±48 μV/K and -343±67

μV/K, respectively. These thermovoltage values are approximately half of those measured for P3HT/BBL (-625±39 μV/K) and PBTTT/BBL (-612±84 μV/K) bilayers, suggesting a higher charge density, which is consistent with the conductivity measurements. The negative Seebeck coefficients of the bilayer films also suggests that the conductivity is dominated by the n-type BBL.

It is of particular interest to determine to which extent also the hole channel contributes to the conduction. The conductivity and Seebeck coefficient of BBL and P($g_4$2T-T) change under oxygen exposure (Supplementary Fig. 13), an evolution that can consistently be interpreted in terms of a 2-layer system composed of two parallel channels for electron and hole transport, respectively. Upon exposure to oxygen, an exponential decrease in conductivity is observed. This decrease is entirely dominated by a reduction in conductivity of the BBL phase (σ_{BBL}), such that the weight factor of the only linearly increasing S_{BBL} will diminish. This shifts the balance towards the positive $S_{P(g42T-T)}$, the weight factor of which will likely increase. As this process continues, the total thermovoltage changes sign and the resulting conductivity starts to increase again when the p-doping of P($g_4$2T-T) becomes large enough to compensate for the conductivity loss in BBL (see Supplementary Fig. 13 for further discussion).

To gain further insight into the fraction of charges that contribute to transport, we paired temperature-dependent resistance measurements with kinetic Monte Carlo (kMC) modelling. kMC simulations are a powerful tool to obtain detailed insight into charge and energy transport in disordered media[39-42]. Fig. 3 shows the result of such simulations tailored to the description of GSET in a bilayer geometry. In short, the model describes the stochastic motion of discrete electrons and holes on a simple cubic lattice using Miller-Abrahams hopping rates. The simulation box includes the bilayer interface in the xy-plane and is chosen sufficiently large to reach flat-band conditions at the boundaries at z = 0 and z = 36 nm. All

Coulomb interactions between charge carriers are explicitly accounted for and updated after each hopping event. There are no traps or static charges, corresponding to *e.g.* dopant ions, in the simulations. For simplicity, equal disorder and hopping parameters are used for electrons and holes. The simulations indicate that the charges are confined to a narrow, essentially single unit cell wide bilayer with equal densities of electrons and holes (see the concentration profiles in Supplementary Fig. 14). The latter is a direct consequence of charge conservation and the nature of the electron transfer process. Despite their relative simplicity, the simulations also quasi-quantitatively reproduce the experimentally observed trends in sheet resistance (Fig. 3a) and activation energy (Fig. 3b) as a function of the vacuum level shift. Specifically, a simulated activation energy of ~100 meV (Supplementary Fig. 15) for vacuum level shifts around 0.5 eV agrees well with the values of 120±15 meV measured for P($g_4$2T-T)/BBL interfaces. Note also that for smaller shifts of the vacuum level (< 0.4 eV), the activation energy exceeds 150 meV, which is in agreement with the larger activation energies measured for P3HT/BBL and PBTTT/BBL systems. Likewise, the range of sheet resistances obtained in kMC simulations matches very well with the values in Fig. 2b, running from ~4 MΩ/sq., for the most conductive blend (highest vacuum level shift), to ~500 MΩ/sq., for the least conductive blend.

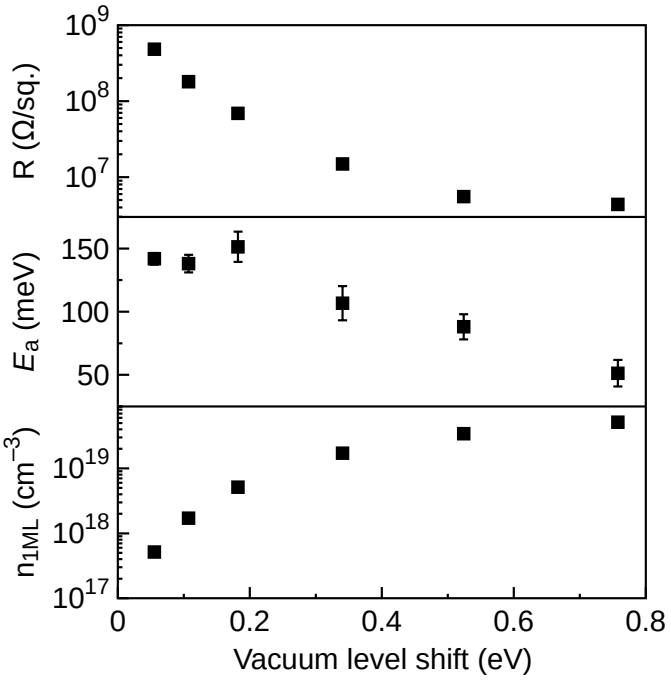

Fig. 3 | Kinetic Monte Carlo simulation of GSET heterojunctions. Calculated resistivity (**a**), activation energy (**b**) and charge density (**c**) vs vacuum level shift for a single bilayer. To facilitate comparison with experiment, the charge density in **c** is calculated by assuming the total charge density sits in a single unit cell wide layer, cf. Supplementary Fig. 15. Parameters used are energetic disorder 60 meV, lattice constant 1.8 nm, attempt to hop frequency 3×10^{14} s^{-1}, all typical for doped conjugated polymes[41].

Electron Paramagnetic Resonance (EPR) spectroscopy was performed to confirm the existence of polarons in the bilayer films and to determine their density. All samples were sealed in EPR tubes inside a nitrogen-filled glovebox to avoid oxygen exposure. The volume-normalized EPR data are reported in Fig. 4a. Separate single-layer polymers show weak EPR signals (Supplementary Fig. 16 and Table 1), whereas a stronger EPR signal intensity is observed for the P($g_4$2T-T)/BBL and P($g_4$2T-TT)/BBL bilayers, consistent with the presence of GSET-induced polarons that have a density of 4–5×10^{19} cm^{-3} (considering a 2 nm-thin interfacial layer as inferred from kMC simulations). This charge density corresponds well to the outcome of the kMC simulations reported above and with what is observed from

impedance measurements (Supplementary Fig. 17), giving values of 7.5×10^{19} cm^{-3} for the P($g_4$2T-T)/BBL sample. For comparison, P3HT/BBL bilayers only give a carrier density of 3.5×10^{18} cm^{-3}, which is in line with the roughly exponential relationship between vacuum level shift and charge carrier density predicted by kMC.

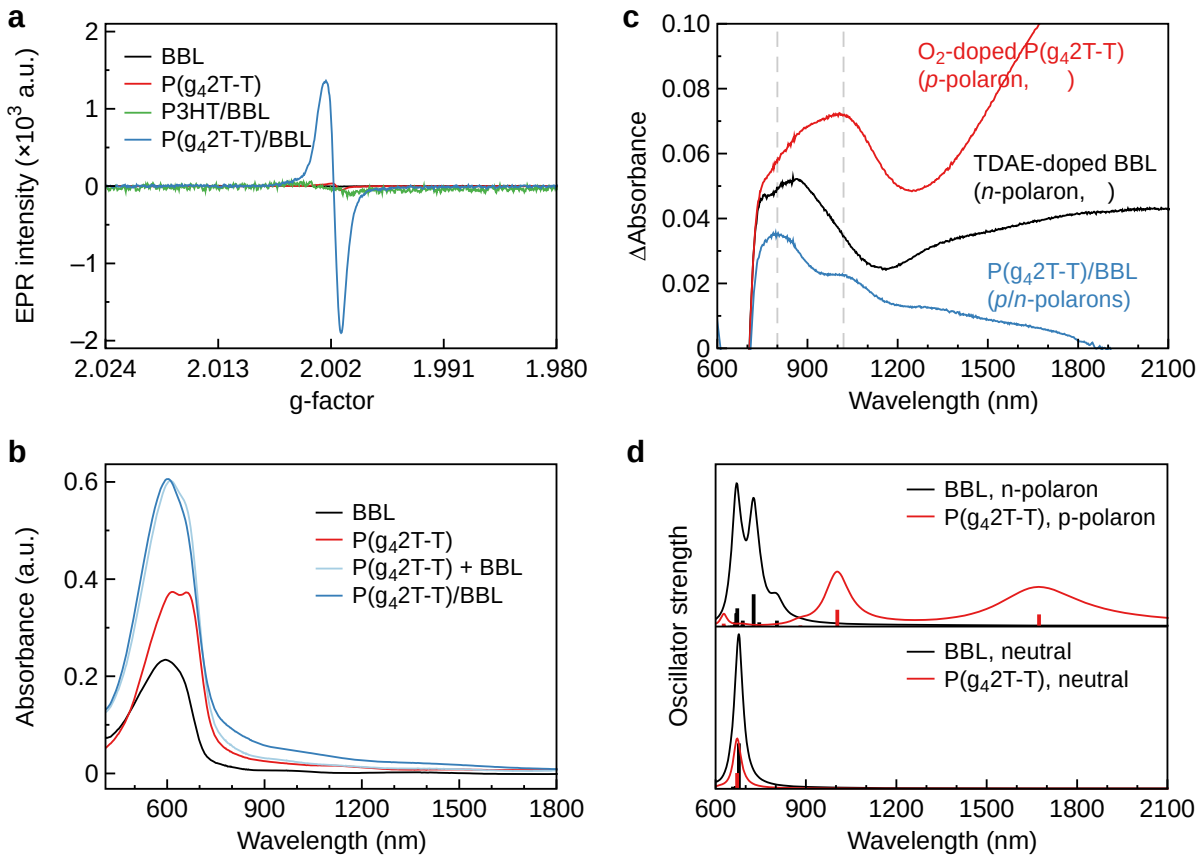

Fig. 4 | GSET confirmed by EPR and UV-Vis-NIR spectroscopies. a, Volume normalized EPR signal of all polymer films, where a 2-nm-thick interfacial layer is assumed in the bilayer films, *i.e.* 1 nm on either side of the interface. **b,** Absorption spectra of BBL, P($g_4$2T-T) and P($g_4$2T-T)/BBL films. **c**, Difference between the bilayer P($g_4$2T-T)/BBL and the sum of single P($g_4$2T-T) and BBL layer (P($g_4$2T-T) + BBL) absorptions, showing the polaron absorption in the bilayer, as well as difference between both TDAE-doped BBL and O_2-doped P($g_4$2T-T) layer and the relative non-doped layer absorptions, showing the n- and p-polaron spectra, respectively. **d**, DFT/TDDFT computed vertical transition energies and spectra for

neutral species (bottom panel) and charged polaronic species (upper panel), for BBL and P($g_4$2T-T). TDDFT vertical energies are shifted by 0.4 eV, and spectra are computed as a Lorentzian convolution of transition energies with a FWHM of 0.1 eV.

The absorption spectra of BBL, P($g_4$2T-T), and P($g_4$2T-T)/BBL, measured in nitrogen atmosphere, are shown in Figs. 4b and 4c together with the computed (density functional theory – DFT, and time-dependent – TDDFT) vertical electronic transitions and spectra for the neutral and single charged states (*i.e.*, polaron) of the corresponding oligomers shown in Fig. 4d. P($g_4$2T-TT) and P($g_4$2T-TT)/BBL absorption spectra are qualitatively similar to P($g_4$2T-T) and P($g_4$2T-T)/BBL, and for this reason are reported in Supplementary Fig. 18. The sum of the pristine BBL and P($g_4$2T-T) absorptions matches the absorption of the bilayer film with respect to the π-π* transition regions of the individual polymers located around 600 nm[37,43]. The optical absorption of polaronic species formed in the bilayer sample was obtained by subtracting the sum of the pristine BBL and P($g_4$2T-T) absorptions from the absorption of the P($g_4$2T-T)/BBL bilayer and is given as the blue curve in Fig. 4c. The absorption of the polarons in the bilayer has two sub-bandgap peaks at 800 and 1030 nm, respectively, with a minor absorption component extending into the mid-infrared (MIR) region, along with a bleaching of the ground state absorption at shorter wavelengths. These two peaks originate from the negative (800 nm) and positive (1030 nm) polarons (Supplementary Fig. 19). The energetics of the polarons are in agreement with the DFT/TDDFT computed spectra of electronically neutral and charged oligomer chains (Fig. 4d). For BBL, one intense transition is computed for the n-polaron species (negatively charged state, q = –1, doublet) and appears at around 800 nm (Fig. 4d)[44]. For both P($g_4$2T-T) and P($g_4$2T-TT) (see Supplementary Fig. 19c for the latter), two main intense transitions are computed for the p-polaron species (positive charged state, q = 1, doublet), namely at *circa* 1000 nm and 1600-1700 nm. The n-

polaron transition (800 nm) and the two p-polaron transitions (1000 nm and 1600-1700 nm) match well with the observed polaron absorption bands in the bilayer structure. Details concerning the nature of the electronic transitions and the polarons' molecular structure are reported in the Supplementary Information.

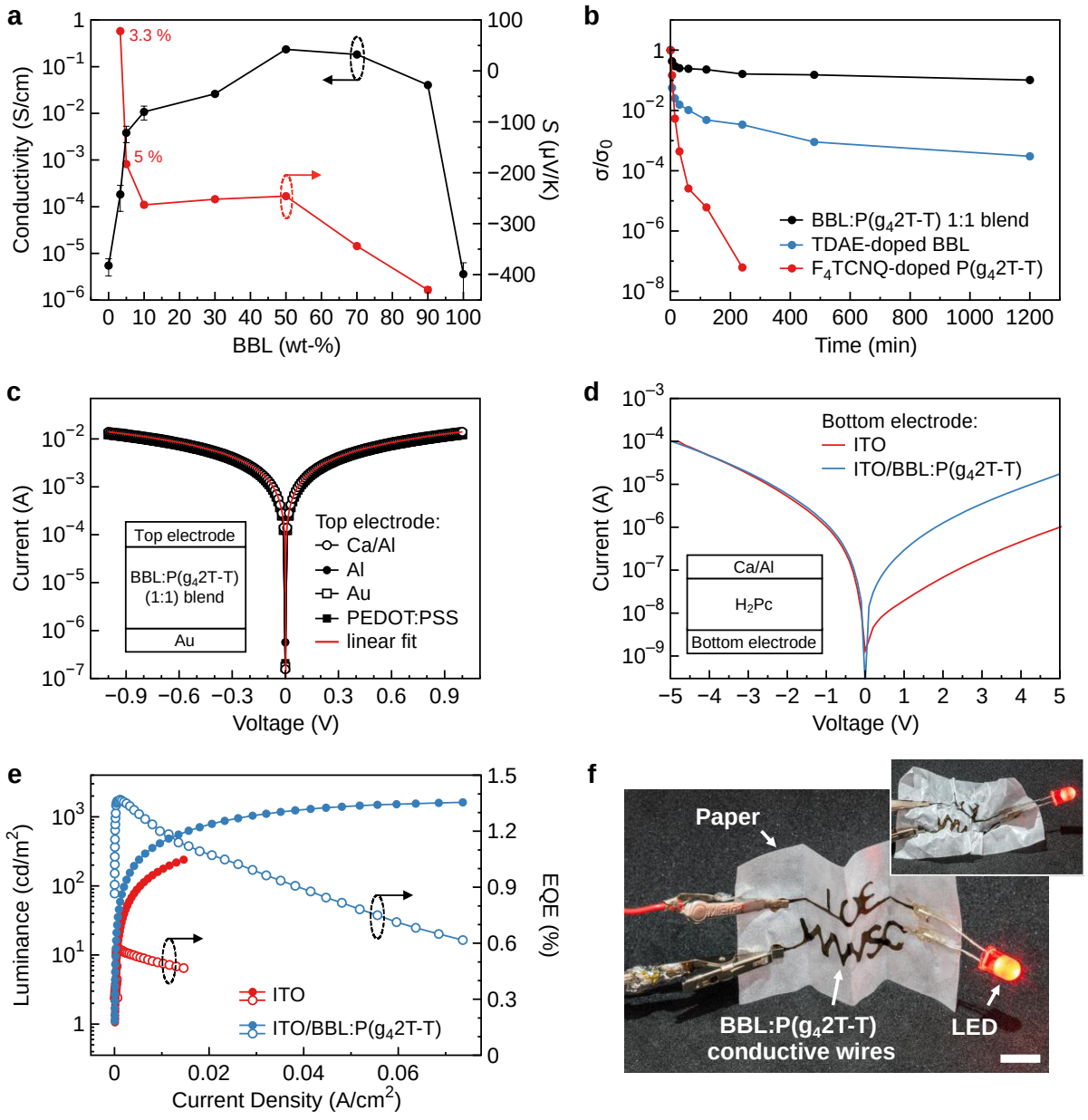

Fig. 5 | Electrical characterization of BBL:P(g42T-T) blend films. a, Conductivity and Seebeck coefficient of BBL:P(g42T-T) blend films at different BBL content; error bars represent standard deviation. **b**, Normalized electrical conductivity of P(g42T-T):BBL 1:1

blend, TDAE-doped BBL and F_4TCNQ-doped P($g_4$2T-T) films upon continuous thermal annealing at 200 °C for 20 h inside a N_2-filled glovebox. **c**, I–V characteristics of BBL:P($g_4$2T-T) (1:1) BHJs sandwiched between Au and various metal electrodes with WFs ranging from 5.1 eV (PEDOT:PSS) to 2.8 eV (Ca/Al). **d**, I–V characteristics of a typical diode using ITO with and without BBL:P($g_4$2T-T) (1:1) BHJs as the bottom electrode. **e**, Luminance and external quantum efficiency (EQE) as a function of current density for inverted OLEDs using ITO with and without BBL:P($g_4$2T-T) (1:1) BHJs as the bottom electrode. **f**, Photograph of a folded paper circuit with BBL:P($g_4$2T-T) BHJ conductive wires lighting up a LED. The paper circuit functions even after being aggressively crumpled. Scale bar 8 mm.

Finally, we demonstrate GSET in D-A bulk heterojunctions (BHJs) by blending P($g_4$2T-T) with BBL in a common solvent. The resulting all-polymer D-A BHJs have appreciable conductivity without the need of heterogeneous dopants. The conductivity of the BHJ layer at different polymer weight ratios is reported in Fig. 5a. A BBL:P($g_4$2T-T) blend with 1:1 weight ratio shows the highest bulk conductivity of 0.23±0.02 S/cm, which is 4–5 orders of magnitude higher than that of the pure polymers. The Seebeck coefficient for these blends varies from -430 μV/K at 90 wt-% BBL to 80 μV/K at 3.3 wt-% BBL, indicating that P($g_4$2T-T) starts to dominate the conduction only at very low BBL concentrations (Fig. 5a). A plateau in the Seebeck coefficient value at around -260 μV/K is found for BBL:P($g_4$2T-T) blend ratios ranging from 10 to 50 wt-%, which is comparable to the thermovoltage of a bilayer made from the same material combination (Fig. 2d). A similar trend is observed for BBL:P($g_4$2T-TT) (Supplementary Fig. 20). This suggests that the interfacial regions at these compositions of the BHJ behave similarly to a bilayer, implying that the balance of p- and n-transport of charge and energy is similar to the bilayer. Weakly diffracting domains with a typical phase-separation length scale of 40–60 nm are observed for 50–70 wt-% BBL content

(Supplementary Figs. 21 and 22). In the BHJ case, the larger interfacial area per unit volume not only increases the bulk conductivity but also impacts the Seebeck coefficient. A maximum power factor of 2.2±0.2 μW/mK^2 was obtained for the BHJs with a BBL content of 70 wt-% (Supplementary Fig. 23), which is among the highest power factors reported for solution processed films of n-type polymers[45]. Since the thermopower values in the electron- and hole-carrying phases counteract each other, the measured high thermopower is not a trivial result. It reflects that, at least for the present material combination, at equal electron and hole densities, the electron charge and energy transport dominates over the hole transport[41]. Strikingly, the all-polymer D-A BHJs show also superior thermal stability as compared to the equivalent single polymer films doped by molecular dopants (Fig. 5b). The electrical conductivity of the BBL:P(g$_4$2T-T) (1:1) blend decreases by less than one order of magnitude upon continuous thermal annealing at 200 °C for 20 h, while for TDAE-doped BBL the conductivity drops by more than four orders of magnitude under the same stressing conditions. The conductivity of F$_4$TCNQ-doped P(g$_4$2T-T) vanishes below detection limits after only 4 h of annealing at 200 °C, which we ascribe to sublimation of the dopant (Supplementary Fig. 24).

Lastly, we investigated the ability of all-polymer D-A BHJs to function as universal interface/transport layers. The BBL:P(g$_4$2T-T) (1:1) blend forms an ohmic contact to various metal electrodes with WFs ranging from 5.1 eV (PEDOT:PSS) to 2.8 eV (Ca/Al), as indicated by the linear I–V characteristics shown in Fig. 5c. When coated onto ITO substrates, BBL:P(g$_4$2T-T) BHJs can effectively inject electrons into a 100-nm-thick layer of phthalocyanine (H$_2$Pc, EA = 2.7 eV), yielding a tenfold higher current level as compared to identical devices with bare ITO electrodes (Fig. 5d). We then tested these all-polymer D-A BHJs as injecting electrodes in proof-of-concept organic light-emitting diodes (OLEDs). Inverted OLEDs with BBL:P(g$_4$2T-T)-coated ITO electrodes (see Methods for detailed

information) yield a higher luminance and external quantum efficiency (EQE) as compared to identical devices without BBL:P($g_4$2T-T) BHJs (Fig. 5e). Because of their appreciable conductivity and ability to make ohmic contacts, these all-polymer D-A BHJs can be printed on paper to form conductive lines and used to light up an inorganic LED, even after being crumpled (Fig. 5f).

In summary, we report GSET in all-polymer D-A heterojunctions. We find that placing low-IE conjugated polymers into contact with high-EA counterparts enables the formation of conducting interfaces with resistivity values that are 5–6 orders of magnitude lower than those of the separate single-layer polymers. The increased electrical conductivity originates from two parallel quasi-2D electron and hole sheet distributions reaching a charge concentration per unit area of ~10^{13} cm^{-2}. UPS, EPR, and UV-Vis-NIR measurements, combined with DFT calculations and kMC simulations, reveal the formation of p/n-polarons induced by a spontaneous electron transfer at the D-A heterointerfaces. We further transferred the concept of GSET to 3D all-polymer bulk heterojunctions, displaying strikingly superior thermal stability as compared to the equivalent single polymer films doped by molecular dopants. We anticipate that our discovery of all-polymer GSET will have a similar impact as the discovery of excited state charge transfer in the field of OLEDs and OSCs. As no mobile dopant molecules are used to dope the system, we envisage that our findings will inspire the development of next-generation biocompatible conductors for bioelectronics and wearable (e-textile/e-skin) devices.

Methods

Materials. High molecular weight BBL (η = 11.6 dL/g in methanesulfonic acid (MSA) at 30 ^{o}C, M_w = 60.5 kDa), was synthesized following the procedure reported previously[46]. P($g_4$2T-T) and P($g_4$2T-TT) were synthesized following the procedure reported earlier[19,37]. RR-P3HT

(Sigma-Aldrich), PBTTT-C14 (Merck Chemicals) and P3CPT (Sigma-Aldrich) were used as received.

Sample preparation. High molecular weight BBL was dissolved in methanesulfonic acid (MSA) at room temperature at a concentration of 2 mg/ml. BBL films were fabricated by spin coating on glass at 3000 rpm for 1 min, immediately followed by immersion into (i) isopropanol and (ii) deionized water to remove any residual MSA from the film, as confirmed by FTIR (Supplementary Fig. 25). P($g_4$2T-T) and P($g_4$2T-TT) were dissolved in anhydrous chloroform at a concentration of 5 mg/ml inside an N_2-filled glovebox, whereas P3HT and PBTTT were dissolved in anhydrous chlorobenzene at a concentration of 5 mg/ml inside the glovebox. Note that chloroform does not dissolve the underneath BBL layer (Supplementary Fig. 26). The PBTTT solution was heated on 150 °C hotplate before use to completely dissolve the polymer. The donor polymers were spin coated inside the glovebox at 1000 rpm for 1 min. The as-prepared films were thermally annealed on a hotplate at 120 °C for 0.5 h inside the glovebox. For preparation of the blend films, P($g_4$2T-T) was dissolved in MSA at a concentration of 2 mg/ml under ambient environment, then blended with BBL solutions at different ratios, followed by stirring at ~200 rpm (room temperature) for one night to allow proper mixing. The blend films were prepared by spin coating at 1500-3000 rpm for 1 min to get a final film thickness of around 20 nm. Finally, the blend films were transferred to the glovebox and annealed on a hotplate at 120 °C for 20 min to get rid of residual MSA and oxygen in the film. A clear conductivity increase could be observed after the annealing process. For the MIM diodes, 30-nm-thick BBL:P($g_4$2T-T) (1:1) films were spin-coated on top of pre-patterned gold electrodes (3 nm Cr as adhesion layer). Top metal electrodes were thermally evaporated through shadow mask, yielding a device with active area 0.25 mm^2. PEDOT:PSS (Clevios^{TM} PH1000) top electrode was spin coated on top of the BHJ films. Electron-only diodes were fabricated by evaporating H_2PC (100 nm) onto ITO and ITO

coated with a 10-nm-thick BBL:P(g42T-T) (1:1) layer, followed by thermal evaporation of Ca (10 nm) and Al (100 nm) as top electrode. The device area was 4 mm^2. Inverted OLEDs were fabricated by thermal evaporation and had the following structure: ITO [or ITO/BBL:P($g_4$2T-T) (1:1) (10 nm)]/4,6-bis(3,5-di(pyridin-3-yl)phenyl)-2-methylpyrimidine (60 nm)/coumarin 545T doped in tris-(8-hydroxyquinoline)aluminum 3 wt% (20 nm)/N,N´-di(1-naphthyl)-N,N´-diphenyl-(1,1´-biphenyl)-4,4´-diamine (70 nm)/MoO_3 (5 nm)/Al. The device area was 8 mm^2. The paper circuit was fabricated by drop casting BBL:P($g_4$2T-T) (1:1) from MSA solution (8 mg/ml) on tracing papers through a shadow mask. The MSA was washed with DI water and dried prior to use.

Electrical characterization. Electrical conductivity and the Seebeck coefficients were measured inside the glovebox using a semiconductor characterization system (Keithley 4200-SCS). For the conductivity measurements, pre-patterned substrates were prepared by thermally evaporating 3 nm of chromium and 20 nm of gold on clean glass substrates with a shadow mask. The substrates had a channel length of 30 μm and a channel width of 1000 μm are used. A pair of Peltier elements were used to provide a temperature difference for Seebeck coefficient measurements. For these measurements, a different shadow mask was used, with a channel length of 0.5 mm and a channel width of 15 mm. The temperature difference was monitored using thermocouples. Electrical characterization of the MIM and electron-only diodes was performed with Keithley 4200 SCS inside a nitrogen filled glovebox. The OLED electrical characterization was carried out by mean of Keithley 2400 source meter, while spectra and brightness properties are measured with HORIBA PR-650 SpectraScan, controlled by a Labview program.

Ultraviolet Photoelectron Spectroscopy. UPS experiments were carried out using a Scienta ESCA 200 spectrometer in ultrahigh vacuum ($1x10^{-10}$ mbar) with a standard helium-discharge lamp with photon energy of 21.22 eV (He I). The total energy resolution of the UPS

measurement is about 80 meV as estimated from the width of the Fermi level of clean gold foil. All spectra were collected at a photoelectron takeoff angle of 0° (normal emission) at room temperature. The work function of the films was extracted from the determination of the high binding-energy cutoff of the UPS spectrum by applying a bias of -3 V to the sample.

Low-Energy Inverse Photoelectron Spectroscopy. For the LEIPS measurements, HWBBL was spin-coated at the rate of 3000 and 4000 rpm from a 2 mg/ml solution. Since the obtained electron affinities are sensitive to the film thickness, we examined two different films to confirm the results. The specimen was introduced into the vacuum chamber evacuated to 3×10^{-7} Pa. The details of the LEIPS apparatus are described elsewhere[47]. An electron beam was introduced to the sample surface and the emitted photons were observed by a photon detector consisting of a bandpass filter and photomultiplier (Hamamatsu R585s). The electron energy was swept in the range between 0 and 5 eV. The overall resolution was between 0.3 and 0.4 eV. No discernible change due to sample damage was observed. The vacuum level was obtained from the inflection point of the sample current.

Electron Paramagnetic Resonance. Quantitative EPR experiments were performed at the Swedish Interdisciplinary Magnetic Resonance Centre (SIMARC) at Linköping University, using a Bruker Elexsys E500 spectrometer operating at about 9.8 GHz (X-band). EPR spectra were recorded in dark at room temperature. The films were prepared by spin-coating on quartz glass as mentioned previously, followed by annealing on a hotplate at 150 °C for 20 min. All samples were encapsulated in an EPR tube with photo active glues inside a glovebox to avoid oxygen exposure.

Thin-film morphology characterization. Atomic Force Microscopy (Digital Instruments) was performed in tapping mode using a silicon cantilever having a spring constant of 40 N/m. Grazing-incidence wide-angle X-ray scattering measurements were performed at Beamline 8-ID-E[48] at the Advanced Photon Source (APS) at Argonne National Laboratory. Samples were

irradiated with a 10.9 keV X-ray beam at an incidence angle of 0.125° to 0.135° in vacuum for two summed exposures of 2.5 s (totaling 5 s of exposure), and scattered X-rays were recorded by a Pilatus 1 M detector located 228.16 mm from the sample at two different heights. The collected images were then processed by using the GIXGUI[49] software written for Matlab and combined to eliminate gaps due to rows of inactive pixels, which also demonstrated that scattering was not changed by the X-ray exposure. All the films used for GIWAXS characterization had the same thickness of ca. 25 nm. The data with incident angle 0.135° was judged to have the best signal and was selected for further analysis. Transmission electron microscope (TEM) lamellas were prepared using a combined focused ion beam – scanning electron microscope (Tescan GAIA3, FEI Versa). A representative area was selected and an initial protective layer of Pt was deposited on top of the region using electron beam-induced deposition with an electron beam of 3 kV. This was followed by ion beam induced deposition to further increase the thickness of the Pt protection layer using a 30 kV Ga^+ ion beam with a current of 153 pA. A lamella was subsequently milled out and lifted to a TEM half-grid[50]. TEM analysis was performed using a FEI Titan 80-300 operated in scanning TEM (STEM) mode at 300 kV and a JEOL NeoARM200F – Mono 40-200 operated in STEM mode at 60 kV and 200 kV acceleration voltages. Energy dispersive X-ray spectroscopy (EDX) and electron energy-loss spectroscopy (EELS) spectral images were acquired to study the spatial distribution oxygen and nitrogen. These signals carried information about the location of BBL and P($g_4$2T-T). The signal was accumulated over multiple scan cycles in order to reduce damage to the sample.

UV-Vis-NIR and FTIR absorption spectroscopy. Absorption spectra of the films were measured using a UV-Vis-NIR spectrophotometer (PerkinElmer Lambda 900) inside an airtight sample holder. The films were prepared on calcium fluoride windows by spin coating, following the above-mentioned procedure. The FTIR spectra were measured in transmission

mode inside an air-tight sample holder with a Bruker Equinox 55 spectrometer averaging 200 scans with a resolution of 4 cm^{-1} and a zerofilling factor of 2.

Thermogravimetric analysis. Thermal stability measurements were performed by TGA with a Mettler Toledo TGA / DSC 3+ under a 20 mL min^{-1} nitrogen flow. A drying step was performed at 50 °C for 10 minutes, after which the weight loss of each sample was recorded from 25 °C to 600 °C with a scan rate of 10 °C min^{-1}.

First principles calculations. Oligomers of different length were considered. For the case of BBL, eight (8) repeat units were considered. For the cases of P($g_4$2T-T) and P($g_4$2T-TT), three (3) repeat units were computed. Each structure was optimized by using the hybrid range-separated-corrected DFT functional, namely ωB97X-D3, combined with double-zeta split valence polarized Pope's basis set 6-31G*. Neutral and charged (positive – q = +1, and negative – q = -1) electronic states were considered. Charged states (*i.e.*, polarons) were initially described using the spin polarized unrestricted DFT (UDFT) approach. For each case, a wavefunction stability check was run using the broken-symmetry (BS)-UDFT scheme. If an instability in the wavefunction was found, both the electronic and nuclear structures were re-optimized following the BS-UDFT potential energy profile. For the case of BBL, an instability in the negatively charged states was found[43,44], while for P($g_4$2T-T) and P($g_4$2T-TT) the unrestricted DFT wavefunction does not show any broken-symmetry behavior. Vertical transition energies were computed for both neutral (TDDFT method) and charged (TDUDFT) states. For BBL, TD-BS-UDFT method was applied. All calculations were performed with the program package Gaussian16 B.01[51].

Acknowledgements

The authors are thankful to Chiara Musumeci (Linköping University) for assistance with AFM and Stefan Gustafsson (Chalmers) for assistance with TEM specimen preparation. This work was supported by the Knut and Alice Wallenberg foundation, VINNOVA (2015-04859), the Swedish Research Council (grant agreements no. 2016-03979, 2016-06146, 2016-05498, 2016-05990, 2018-03824), the Swedish Government Strategic Research Area in Materials Science on Functional Materials at Linköping University (Faculty Grant SFO Mat LiU no. 2009 00971), ÅForsk (18-313), and the European Research Council (ERC) under grant agreement no. 637624. We also wish to thank Chalmers Material Analysis Laboratory for their support of microscopes. T.P.R gratefully acknowledges funding from the Finnish Cultural Foundation and the Finnish Foundation for Technology Promotion. N.S. thanks the National Natural Science Foundation of China (grant no. 61805211). Work at the University of Washington was supported by the National Science Foundation (DMR-1708450). D.F. acknowledges the Deutsche Forschungsgemeinschaft (DFG) for the grant "Molecular Understanding of Thermo-Electric Properties in Organic Polymers" (FA 1502/1-1), and the Regional Computing Centre (RRZK) of Universität zu Köln, for providing computing time and resources on the HPC CHEOPS.

Author contributions

S.F. conceived, designed and supervised the project. H.S. initiated the study. K.X. and H.S. prepared the samples, performed the electrical measurements and analyzed the data. T.P.R. recorded and analyzed the UV-vis-NIR data. G.W. performed the GIWAXS and AFM measurements. R.K. synthesized P($g_4$2T-T) and P($g_4$2T-TT). N.B.K. synthesized BBL. Y.P. performed and analyzed the EPR data. X.L. recorded and analyzed the UPS spectra. D.F. performed the DFT calculations. K.S. and H.Y. performed the LEIPS measurements and analyzed the data. C.Y.Y fabricated and tested the paper circuits. N.S. fabricated and tested

the OLEDs. G.P. and A.B.Y performed the TEM analysis. M.K. performed the kMC simulations. K.X., H.S., M.K., C.M., and S.F. wrote the manuscript. E.O. W.M.C., M.F., S.A.J., M.B. and all the authors contributed to the data analysis, discussion and manuscript preparation.

Competing interests

The authors declare no competing financial interests.

Data availability

The authors declare that the main data supporting the findings of this study are available within the article and its Supplementary Information files. Additional data are available from the corresponding authors upon request.

References

1. Reineke S, Thomschke M, Lussem B, Leo K. White organic light-emitting diodes: Status and perspective. *Rev. Mod. Phys.* **85,** 1245-1293 (2013).
2. Peumans P, Yakimov A, Forrest SR. Small molecular weight organic thin-film photodetectors and solar cells. *J. Appl. Phys.* **93,** 3693-3723 (2003).
3. Lussem B, Keum CM, Kasemann D, Naab B, Bao ZN, Leo K. Doped Organic Transistors. *Chem. Rev.* **116,** 13714-13751 (2016).
4. Bubnova O, Crispin X. Towards polymer-based organic thermoelectric generators. *Energy Environ. Sci.* **5,** 9345-9362 (2012).
5. Walzer K, Maennig B, Pfeiffer M, Leo K. Highly Efficient Organic Devices Based on Electrically Doped Transport Layers. *Chem. Rev.* **107,** 1233-1271 (2007).

6. Bubnova O, Khan ZU, Wang H, Braun S, Evans DR, Fabretto M, *et al.* Semi-metallic polymers. *Nat. Mater.* **13,** 190-194 (2014).

7. Russ B, Glaudell A, Urban JJ, Chabinyc ML, Segalman RA. Organic thermoelectric materials for energy harvesting and temperature control. *Nat. Rev. Mater.* **1,** 16050 (2016).

8. Salzmann I, Heimel G, Oehzelt M, Winkler S, Koch N. Molecular Electrical Doping of Organic Semiconductors: Fundamental Mechanisms and Emerging Dopant Design Rules. *Acc. Chem. Res.* **49,** 370-378 (2016).

9. Rivnay J, Inal S, Salleo A, Owens RM, Berggren M, Malliaras GG. Organic electrochemical transistors. *Nat. Rev. Mater.* **3,** 17086 (2018).

10. Sun H, Vagin M, Wang S, Crispin X, Forchheimer R, Berggren M, *et al.* Complementary Logic Circuits Based on High-Performance n-Type Organic Electrochemical Transistors. *Adv. Mater.* **30,** 1704916 (2018).

11. Nardes AM, Kemerink M, Janssen RAJ, Bastiaansen JAM, Kiggen NMM, Langeveld BMW, *et al.* Microscopic understanding of the anisotropic conductivity of PEDOT : PSS thin films. *Adv. Mater.* **19,** 1196-1200 (2007).

12. Qiu L, Liu J, Alessandri R, Qiu X, Koopmans M, Havenith Remco WA, *et al.* Enhancing doping efficiency by improving host-dopant miscibility for fullerene-based n-type thermoelectrics. *J. Mater. Chem. A* **5,** 21234-21241 (2017).

13. Pingel P, Neher D. Comprehensive picture of p-type doping of P3HT with the molecular acceptor F4TCNQ. *Phys. Rev. B* **87,** 115209 (2013).

14. Zuo G, Abdalla H, Kemerink M. Impact of doping on the density of states and the mobility in organic semiconductors. *Phys. Rev. B* **93,** 235203 (2016).

15. Li J, Koshnick C, Diallo SO, Ackling S, Huang DM, Jacobs IE, *et al.* Quantitative Measurements of the Temperature-Dependent Microscopic and Macroscopic Dynamics of a Molecular Dopant in a Conjugated Polymer. *Macromolecules* **50,** 5476-5489 (2017).

16. Li J, Rochester CW, Jacobs IE, Friedrich S, Stroeve P, Riede M, *et al.* Measurement of Small Molecular Dopant F4TCNQ and C60F36 Diffusion in Organic Bilayer Architectures. *ACS Appl. Mater. Interfaces* **7,** 28420-28428 (2015).

17. Hynynen J, Kiefer D, Yu LY, Kroon R, Munir R, Amassian A, *et al.* Enhanced Electrical Conductivity of Molecularly p-Doped Poly(3-hexylthiophene) through Understanding the Correlation with Solid-State Order. *Macromolecules* **50,** 8140-8148 (2017).

18. Jacobs IE, Moulé AJ. Controlling Molecular Doping in Organic Semiconductors. *Adv. Mater.* **29,** 1703063 (2017).

19. Kroon R, Kiefer D, Stegerer D, Yu L, Sommer M, Müller C. Polar Side Chains Enhance Processability, Electrical Conductivity, and Thermal Stability of a Molecularly p-Doped Polythiophene. *Adv. Mater.* **29,** 1700930 (2017).

20. Reiser P, Muller L, Sivanesan V, Lovrincic R, Barlow S, Marder SR, *et al.* Dopant Diffusion in Sequentially Doped Poly(3-hexylthiophene) Studied by Infrared and Photoelectron Spectroscopy. *J. Phys. Chem. C* **122,** 14518-14527 (2018).

21. Fahlman M, Fabiano S, Gueskine V, Simon D, Berggren M, Crispin X. Interfaces in organic electronics. *Nat. Rev. Mater.* **4,** 627-650 (2019).

22. Alves H, Molinari AS, Xie HX, Morpurgo AF. Metallic conduction at organic charge-transfer interfaces. *Nat. Mater.* **7,** 574-580 (2008).

23. Odom SA, Caruso MM, Finke AD, Prokup AM, Ritchey JA, Leonard JH, *et al.* Restoration of Conductivity with TTF-TCNQ Charge-Transfer Salts. *Adv. Funct. Mater.* **20,** 1721-1727 (2010).

24. Hiraoka M, Hasegawa T, Yamada T, Takahashi Y, Horiuchi S, Tokura Y. On-Substrate Synthesis of Molecular Conductor Films and Circuits. *Adv. Mater.* **19,** 3248-3251 (2007).

25. Jacobs IE, Cendra C, Harrelson TF, Valdez ZIB, Faller R, Salleo A, *et al.* Polymorphism controls the degree of charge transfer in a molecularly doped semiconducting polymer. *Mater. Horiz.* **5,** 655-660 (2018).

26. Jérome D. Organic Conductors: From Charge Density Wave TTF−TCNQ to Superconducting (TMTSF)2PF6. *Chem. Rev.* **104,** 5565-5592 (2004).

27. Chen XL, Jenekhe SA. Bipolar Conducting Polymers: Blends of p-Type Polypyrrole and an n-Type Ladder Polymer. *Macromolecules* **30,** 1728-1733 (1997).

28. Grancini G, Maiuri M, Fazzi D, Petrozza A, Egelhaaf HJ, Brida D, *et al.* Hot exciton dissociation in polymer solar cells. *Nat. Mater.* **12,** 29-33 (2013).

29. Kawamura Y, Yanagida S, Forrest SR. Energy transfer in polymer electrophosphorescent light emitting devices with single and multiple doped luminescent layers. *J. Appl. Phys.* **92,** 87-93 (2002).

30. Yoshida H. Principle and application of low energy inverse photoemission spectroscopy: A new method for measuring unoccupied states of organic semiconductors. *J. Electron. Spectrosc. Relat. Phenom.* **204,** 116-124 (2015).

31. Yoshida H. Near-ultraviolet inverse photoemission spectroscopy using ultra-low energy electrons. *Chem. Phys. Lett.* **539-540,** 180-185 (2012).

32. Oehzelt M, Koch N, Heimel G. Organic semiconductor density of states controls the energy level alignment at electrode interfaces. *Nat. Commun.* **5,** 4174-4174 (2014).

33. Greiner MT, Helander MG, Tang W-M, Wang Z-B, Qiu J, Lu Z-H. Universal energy-level alignment of molecules on metal oxides. *Nat. Mater.* **11,** 76-81 (2012).

34. Bokdam M, Çakır D, Brocks G. Fermi level pinning by integer charge transfer at electrode-organic semiconductor interfaces. *Appl. Phys. Lett.* **98,** 113303-113303 (2011).

35. Braun S, Salaneck WR, Fahlman M. Energy-Level Alignment at Organic/Metal and Organic/Organic Interfaces. *Adv. Mater.* **21,** 1450-1472 (2009).

36. Bao Q, Braun S, Wang C, Liu X, Fahlman M. Interfaces of (Ultra)thin Polymer Films in Organic Electronics. *Adv. Mater. Interfaces* **6,** 1800897 (2018).

37. Kiefer D, Kroon R, Hofmann AI, Sun H, Liu X, Giovannitti A, *et al.* Double doping of conjugated polymers with monomer molecular dopants. *Nat. Mater.* **18,** 149-155 (2019).

38. Pasveer WF, Cottaar J, Tanase C, Coehoorn R, Bobbert PA, Blom PW, *et al.* Unified description of charge-carrier mobilities in disordered semiconducting polymers. *Phys. Rev. Lett.* **94,** 206601 (2005).

39. Bässler H. Charge Transport in Disordered Organic Photoconductors a Monte Carlo Simulation Study. *Phys. Status Solidi B* **175,** 15-56 (1993).

40. Zuo G, Abdalla H, Kemerink M. Conjugated Polymer Blends for Organic Thermoelectrics. *Adv. Electron. Mater.* **5,** 1800821 (2019).

41. Zuo G, Li Z, Wang E, Kemerink M. High Seebeck Coefficient and Power Factor in n-Type Organic Thermoelectrics. *Adv. Electron. Mater.* **4,** 1700501 (2018).

42. Melianas A, Etzold F, Savenije TJ, Laquai F, Inganäs O, Kemerink M. Photo-generated carriers lose energy during extraction from polymer-fullerene solar cells. *Nat. Commun.* **6,** 8778 (2015).

43. Wang S, Sun H, Ail U, Vagin M, Persson PO, Andreasen JW, *et al.* Thermoelectric Properties of Solution-Processed n-Doped Ladder-Type Conducting Polymers. *Adv. Mater.* **28,** 10764-10771 (2016).

44. Fazzi D, Fabiano S, Ruoko T-P, Meerholz K, Negri F. Polarons in π-conjugated ladder-type polymers: a broken symmetry density functional description. *J. Mater. Chem. C* **7,** 12876-12885 (2019).

45. Yao CJ, Zhang HL, Zhang Q. Recent Progress in Thermoelectric Materials Based on Conjugated Polymers. *Polymers* **11,** 107 (2019).

46. Arnold FE, Van Deusen RL. Preparation and Properties of High Molecular Weight, Soluble Oxobenz[de]imidazobenzimidazoisoquinoline Ladder Polymer. *Macromolecules* **2,** 497-502 (1969).

47. Yoshida H. Note: Low energy inverse photoemission spectroscopy apparatus. *Rev. Sci. Instrum.* **85,** 016101 (2014).

48. Jiang Z, Li XF, Strzalka J, Sprung M, Sun T, Sandy AR, *et al.* The dedicated high-resolution grazing-incidence X-ray scattering beamline 8-ID-E at the Advanced Photon Source. *J. Synchrotron Radiat.* **19,** 627-636 (2012).

49. Jiang Z. GIXSGUI: a MATLAB toolbox for grazing-incidence X-ray scattering data visualization and reduction, and indexing of buried three-dimensional periodic nanostructured films. *J. Appl. Crystallogr.* **48,** 917-926 (2015).

50. Pettersson H, Nik S, Weidow J, Olsson E. A method for producing site-specific TEM specimens from low contrast materials with nanometer precision. *Microsc. Microanal.* **19,** 73-78 (2013).

51. Frisch MJ, Trucks GW, Schlegel HB, Scuseria GE, Robb MA, Cheeseman JR, *et al. Gaussian 16, Revision B.01*. Gaussian, Inc.: Wallingford, CT, USA, (2016).